

# On the detachment mechanisms of monodisperse bubbles flowing through a wavy channel

Reza Azadi and David S. Nobes\*

Applied Thermofluids Lab., University of Alberta, Department of Mechanical Engineering,  
Edmonton, Canada

\* david.nobes@ualberta.ca

## Abstract

The dynamics of breakup and attachment of monodisperse bubbles moving in a viscous liquid in a wavy channel is investigated using particle shadow velocimetry (PSV). A full cycle of a sinusoidal channel with a throat size of 500  $\mu\text{m}$  is fed by a seeded flow of a viscous glycerol/water mixture and a consistent flow of monodisperse air bubbles with sizes larger than the throat size. A sum of correlation particle image velocimetry (SOC-PIV) and standard PIV (sPIV) approaches were used to calculate the two dimensional velocity field of the single phase and two-phase flows, respectively. The results show that bubbles experience three different processes as they pass the throat of the channel: necking, breakup and attachment. The motion of bubbles enforces a positive velocity shift to the surrounding fluid in the streamwise direction in comparison to the single phase liquid flow of the same flow rate. A sudden reduction of the velocity magnitude occurs on the channel centerline as the bubble necks down at the throat of the channel. The bubble finally breaks up and a daughter bubble is born as the result of a large velocity gradient between the front and rear of the bubble. The reduction in the velocity of both daughter bubble and the surrounding liquid continues to a certain minimum value and at the same time the mother bubble accelerates in the wake of the daughter bubble and finally attaches to it. The inception of attachment is followed by a recovery of the velocity field to a similar one as before the onset of necking down.

## 1 Introduction

With a wide range of applications in engineering and natural phenomena (Cubaud & Ho, 2004), the motion of monodisperse bubbles in a continuous fluid flow becomes more complicated while flowing through channels with varying cross-sectional area. Spatial variations in the flow path can induce significant instabilities in velocity and pressure fields of two-phase flows (Zhang et al., 2017a). Wavy or corrugated channels with multiple constrictions in the flow path are commonly used to increase the dissipation rate and improve heat transfer coefficient in microchannels (Sauzade & Cubaud, 2013). Flow paths in porous media can be modelled as simplified wavy channels where investigation of dispersed fluid interaction with its surrounding giving a deeper insight into the phenomenon (Lauga, Stroock, & Stone, 2004).

The experimental observations of Krishna et al. (1999) showed that for channel diameters of more than eightfold the bubble equivalent diameter, the walls of confinement have negligible effect on the dynamic characteristics of rising bubbles. While for aspect ratios smaller than eight, the preliminary effect of confinement would be a significant reduction in rising velocity of bubbles. Zhang et al. (2017b) used  $\text{N}_2$  bubbles in a mixture of glycerol/water with a viscosity range of 26 to 1000 mPa.s to experimentally study the bubble breakup process flowing through a flow-focusing device. Their results reveal that the bubble volume undergoes a linear volume expansion before the breakup that is a function of Capillary number and gas-liquid flow rate ratio. Capillary number is defined as

$Ca = \mu_c U / \sigma$  with  $\mu_c$ ,  $U$  and  $\sigma$  representing dynamic viscosity of continuous phase, characteristic velocity and surface tension coefficient, respectively. The experiments were done using a squared shaped  $400 \mu\text{m} \times 400 \mu\text{m}$  microchannel. They calculated the instantaneous bubble volume assuming a circular cross-section for the bubbles and reported gas flow rates based on these values.

Using digital image processing techniques, Sauzade and Cubaud (2018) investigated the process of dissolution of carbon dioxide bubbles in viscous silicone oils flowing in corrugated microchannels. The ratio of rear to front curvature of individual bubbles was used as a criterion to differentiate between the capillary and viscous regimes. Obtaining the temporal evolution of bubble topology, they could calculate the net mass flux across the interface and showed that dissolution mass transfer coefficient plays an important role in describing diffusion-based multiphase flows in small scale geometries.

A numerical study done by Patel et al. (2019) on the bubble motion passing through sinusoidal channels showed that the rising velocity of bubbles is a function of Reynolds Number, Morton number and amplitude of the wavy wall profile. Reynolds and Morton numbers are defined as  $Re = \rho_c UL / \mu_c$  and  $Mo = g \mu_c^4 \Delta \rho / \rho_c^2 \sigma^3$  with  $\rho_c$ ,  $\Delta \rho$ ,  $g$  and  $L$  defining density of continuous phase, difference of densities of phases, gravitational acceleration and characteristic length. Throat width,  $w_t$ , was used as the characteristic length and the ratio  $\sigma / \mu_c$  and  $w_t \mu_c / \sigma$  were used as velocity and time scales. They simulated single bubbles with equivalent diameters smaller than the throat size for symmetrical channels and channels with offsets. Their results show that for higher Reynolds numbers, the bubble starts to wobble and produce an instability in the rising velocity of bubble. Significant changes in the bubble topology are found to be a function of Bond number ( $Bo = \Delta \rho g L^2 / \sigma$ ). Bubble breakup was reported for several test cases where the amplitude of the wall profile was introduced as the responsible parameter for this phenomenon.

Liu et al. (2016) accomplished a numerical study to investigate the dynamics of bubble breakup passing through a micro T-junction. They identified three different breakup regimes including tunnel, obstructed and combined breakup. For small sizes of bubbles moving in low flow velocities, no breakup was predicted by the model. In all three regimes, bubble extends, squeezes and pinches off before the onset of breakup. The results show that interface of bubble experiences a sudden pressure drop while being squeezed by the bulk flow and while extending in the branches of bifurcation in the tunnel and obstructed breakup regimes. Using the entrance length of the T-junction as the characteristic length, they provided a bubble breakup regime map based on the critical Capillary number and a fitting constant which is a function of viscosity ratio of phases. Their results are in a good agreement with the corresponding experimental data.

The present study aims to identify the dynamics of a highly viscous liquid flow in one cycle of a wavy microchannel as monodisperse bubbles pass through it using the image-based PSV technique. SOC-PIV and sPIV algorithms are used to calculate the velocity fields for single and two-phase flows out of images of seeded liquid fluid recorded by a high-speed camera. The results for one set of flow conditions is given in the current paper and more will be presented at the conference.

## 2 Experimental procedure

To mimic a continuous flow of a transparent viscous liquid fluid, a mixture of 91.92 %wt glycerol/water was used. The density and dynamic viscosity of the solution were calculated to be  $1240 \text{ kg/m}^3$  and  $0.303 \text{ Pa}\cdot\text{s}$ , respectively (Cheng, 2008). Ambient air was chosen as the working fluid for dispersed phase. Experiments were done at room conditions ( $20 \text{ }^\circ\text{C}$ ,  $1 \text{ atm}$ ) with negligible heat transfer between the flow and its surrounding. A schematic of the experimental setup is shown in Figure 1. A syringe pump (PHD 2000, Harvard Apparatus Inc., USA) was used to inject a stable flow of continuous phase to the test section through flexible tubing of  $1 \text{ mm}$  internal diameter (ID). Compressed air was fed into a pressure vessel with a capacity of maximum  $30 \text{ psi}$ , which injected pressurized air into the test section through a stainless steel needle of  $584.2 \mu\text{m}$  ID.

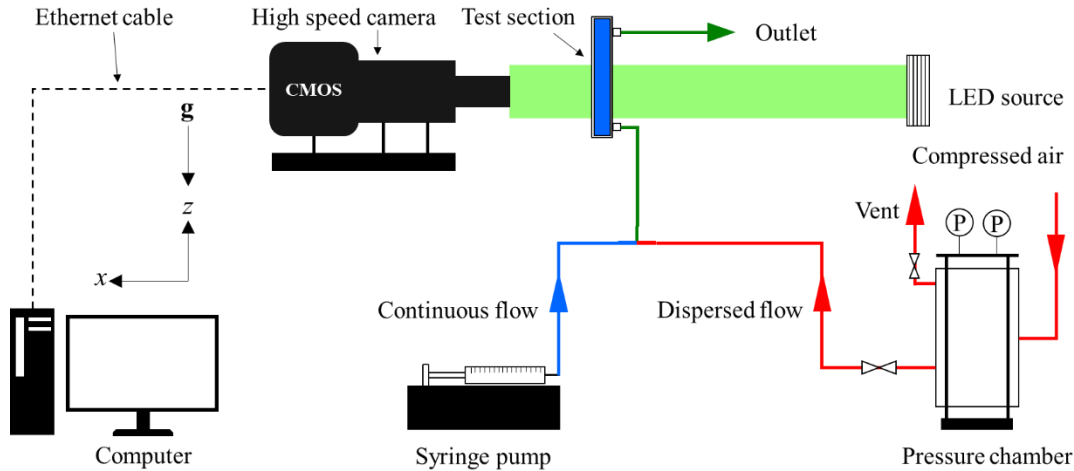


Figure 1: A schematic of the experimental facility

For each set of tests, the flow rate of air was controlled by adjusting the pressure of the vessel that produced a continuous flow of monodisperse bubbles. Figure 2(a) shows the sinusoidal flow cell used for the experiments. The geometry of the flow path was manufactured using an SLS additive manufacturing technique (Form2, FormLabs, USA) with a resolution of 50  $\mu\text{m}$  with clear resin (V4-FLGPCL04, FormLabs, USA) as the base material. Two transparent side windows (5.84 mm thickness, Optix acrylic, Plaskolit Inc., USA) were manufactured utilizing a commercial laser cutter machine (VersaLaser VLD Version 3.50, Universal Laser Systems, USA) which confined the flow in the depth of flow cell while fully displaying the fluid flow inside the channel. To produce a stabilized flow of monodisperse bubbles, both phases encountered in a three-way connection before entering the flow cell. An inlet with diameter of 2 mm was used to feed in the two-phase flow into the channel and an outlet with a similar size was utilized for flow to exit the channel.

The channel walls follow a sinusoidal profile of the form  $y = a [1 - \sin(\pi z/\lambda + \phi)] + w_t/2$  which is limited to  $0 \leq z \leq 2\lambda$ , as shown in Figure 2(b). Here,  $a$  is the wave amplitude,  $\lambda$  defines the wavelength and  $\phi$  is the phase angle. Upstream of the wave section was extended by  $4\lambda$  in a symmetric converging shape to allow the generated bubbles to reach steady state on the centerline before entering the wavy section. In a similar trend, the downstream of the wave profile diverged in a length of  $2\lambda$  and encompasses the channel outlet at the end of the channel. For the current study, the wave parameters were chosen to be  $a = 500 \mu\text{m}$ ,  $\lambda = 5,000 \mu\text{m}$ ,  $\phi = 90^\circ$  and  $w_t = 500 \mu\text{m}$ . The depth of the channel was chosen to be twofold the size of pore throat.

To divulge the characteristics of two-phase flow in the wavy channel, an optical diagnostic system based on PSV technique was utilized as shown in Figure 1. Sphere polymer microbeads with an average size of 10  $\mu\text{m}$  and density of 1,050  $\text{kg}/\text{m}^3$  were distributed uniformly in the continuous phase which resulted in an image sizing of 2 to 5 pixels for the settings of the current experiment. A high speed LED pulsing system (ILA.LPS 3, ILA-5150 GmbH, Germany) illuminated the FOV uniformly and a high speed camera (FASTCAM Mini WX50, Photron Inc., USA) at frame rates of 2 to 3 KHz was employed to capture the shadow of particles and bubble interface. For each experiment, the frame rate of the camera, shutter speed and the light intensity were cautiously chosen to freeze the motion of particles and to create an acceptable intensity distribution. A macro lens (105mm f/2.8, AF MICRO-NIKKOR, Nikon Inc., Japan) coupled to the camera with a bellow extension (Nikon PB-4, Nikon Inc., Japan) was used to acquire higher magnifications of the FOV. Using the bellow extension, increased the magnification while shrinking the depth of field (DOF). A compromise was found between the magnification and DOF for each experimental condition. Depending on the selected frame rate, maximum resolution of the image varied for constant magnification factor, which provided a FOV ranging from  $4.8 \times 9.90 \text{ mm}^2$  (width  $\times$  height) to  $5.12 \times 12.80 \text{ mm}^2$  (width  $\times$  height).

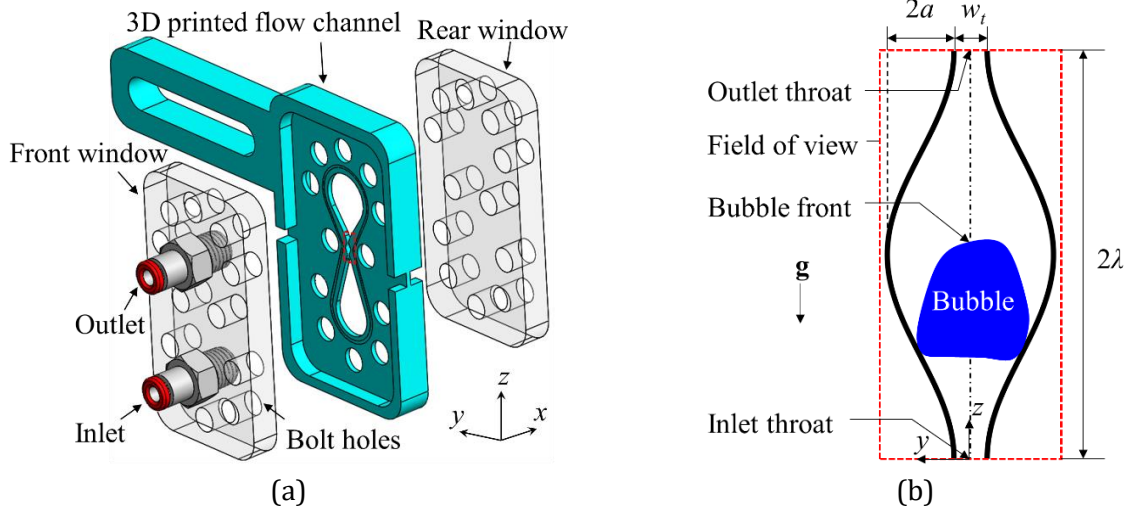


Figure 2: The experimental facility: (a) 3D view of the flow channel, (b) Definition of parameters and annotations corresponding to the wavy channel.

An image processing algorithm was developed (MATLAB R2018b V9.5.10, The Mathworks Inc.) to mask out the interior regions corresponding to the dispersed phase and exterior regions with sinusoidal boundaries. The algorithm comprises adjusting the contrast, image sharpening, binarizing, median filtering, removal of small objects, hole filling, determination of connected components, removal of undesired objects and calculation of properties of final objects. Figure 3 shows the main steps of the image processing algorithm which was applied to a random frame of test data.

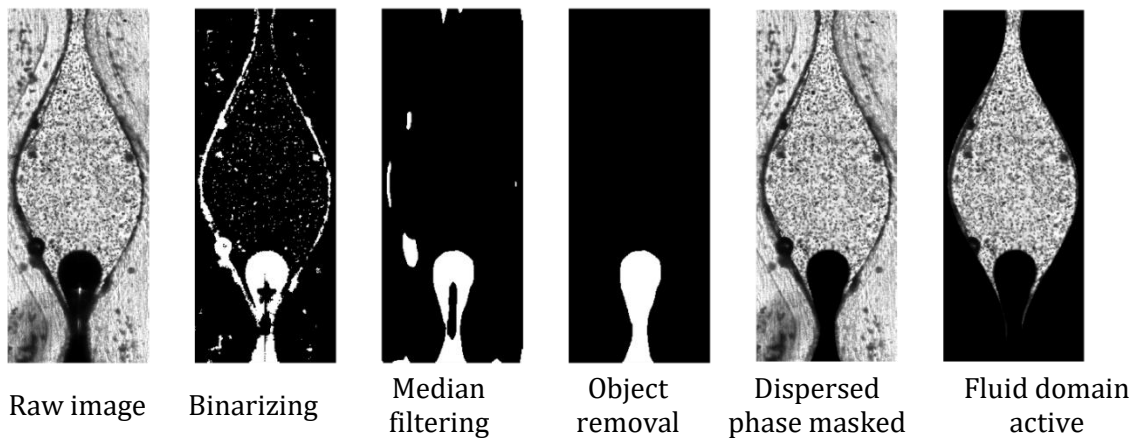


Figure 3: Main image processing steps to detect the gas-liquid interface and to mask out the unwanted regions out of the image.

SOC-PIV and sPIV schemes with commercial software (Davis 10.0.5, LaVision GmbH, Germany) was used to determine the averaged displacement of particles in the continuous phase. This produced a time-averaged field for the single phase and time-resolved fields of velocity vectors for the two-phase flow. Cross-correlation started with  $64 \times 64$  square interrogation windows with 50% overlap and three passes and ended by  $32 \times 32$  square interrogation windows with 87% overlap and five passes to sufficiently resolve the spatial variations of the velocity field. At each step of multi-pass calculations, a median filter with region size of  $3 \times 3$  was applied twice to detect and delete universal outliers. After the calculation of all vectors, a median filter based on the standard deviation was applied to each calculated vector to remove and replace any possible spurious vectors. Finally, a de-noising algorithm based on a first order linear fit with two passes was employed to smooth out the vector field using 32 neighboring vectors for each cell data. The result is a smoothed vector field with a minimum number of spurious vectors.

### 3 Results and discussion

Length and time were non-dimensionalized using the width of the throat,  $w_t$  and the ratio  $w_t\mu/\sigma$  scales the time.  $\bar{U}_{t,av}$  is the spatial (in  $y$  direction) averaged velocity magnitude of outlet throat for the single liquid phase flow and is used to non-dimensionalize the velocity fields. The SOC algorithm was used to calculate the velocity field for the single phase flow case using frames ranging from 800 to 1000 depending on the captured data. The motion and break-up of a single bubble is shown in Figure 4, but is representative of the bubble stream. As the mono-dispersed bubbles move in a wavy channel, they apply velocity and pressure gradients to the bulk fluid by transporting the surrounding liquid in their front and rear. These fluctuations are amplified as the bubble itself experiences a gradient in its velocity due to the change of cross sectional area of the channel.

Bubbles with sizes larger than the throat size are most probable to breakup due to these velocity fluctuations as they pass the narrowest section of the channel, the throats. While the front of bubble enters the throat, it starts to accelerate toward the downstream of channel. At the same time, a large portion of the bubble (rear of bubble) is already competing with the viscous drag forces applied to it by the surrounding liquid, but is not capable of compensating for the lag in acceleration. This difference in the velocity of bubble front and rear causes a stretch in the bubble that continues to the instant at which bubble starts to neck down, then breakup and to finally create a daughter bubble.

Figure 4 shows that the breakup happens at the position where the cross sectional area is minimal. After the breakup, the rear of the newly born daughter bubble, which has already passed the throat, starts to decelerate in a proportionally wider region. At the same time, the front of the new mother bubble, which is located at a narrower region, accelerates in the wake of daughter bubble and finally attaches to it. A snapshot of the instant the mother bubble attaches to the daughter bubble is shown in Figure 4. The results show that mother bubble may or may not coalesce with the daughter bubble after the attachment.

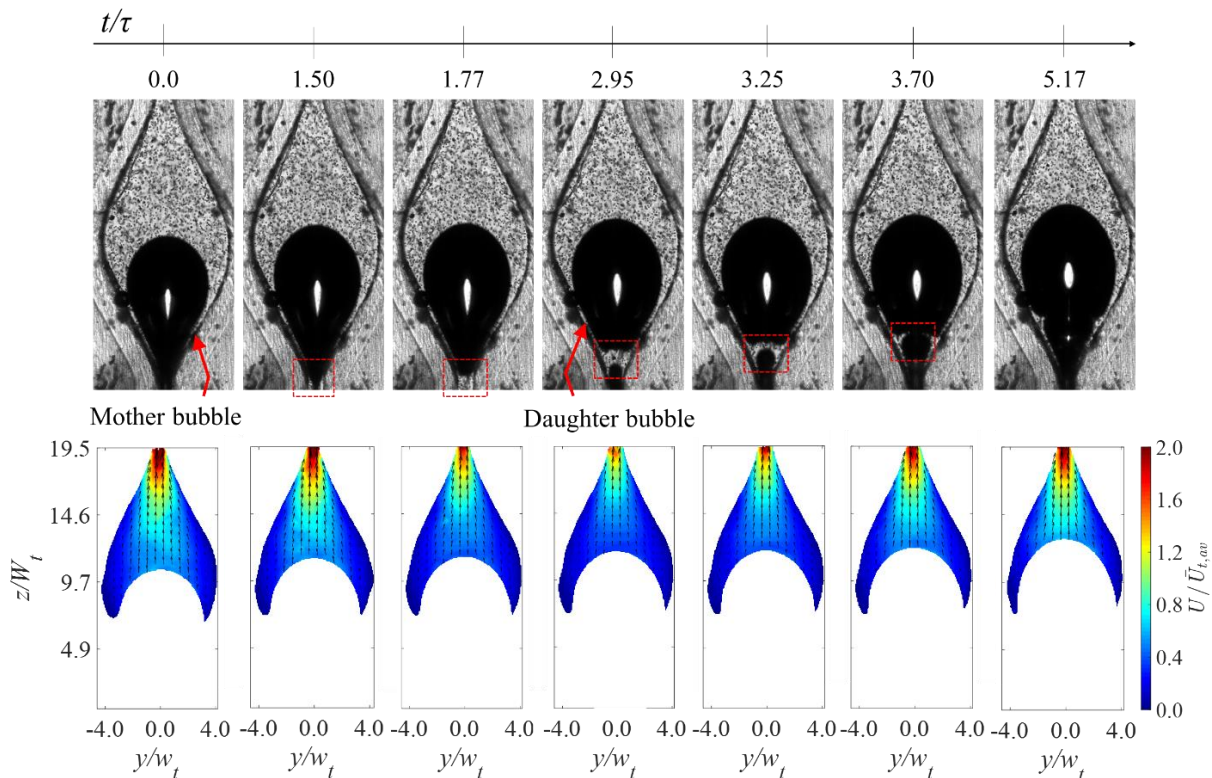


Figure 4: Snapshots of the flow field (1<sup>st</sup> row) and the calculated velocity fields (2<sup>nd</sup> row) (S-PIV) for  $Q_1 = 342$  ml/h at several instants comprising the bubble necking, breakup and attachment.

Figure 5(a) shows the normalized velocity field of the liquid flowing at the rate of  $Q_1 = 342$  ml/h. Liquid flow decelerates as it approaches the wide region in the bulged part of the channel and increases its speed on entering outlet throat. Normalized velocity magnitudes of the centerline are plotted in Figure 5(b) for the instants of necking, detachment (breakup) and attachment onsets in comparison with the velocity magnitude of the single liquid phase. While the bubble expands into the downstream of the throat, it pushes the surrounding liquid upward, imposing a positive velocity shift streamwise. This is shown in Figure 5(b) for the velocity profile on the centerline, at the moment bubble starts necking.

At the instant of the breakup, bubble experiences the maximum tension, where the viscous forces applied to the rear of bubble impose the maximum drag to the bubble surface and reduces its speed. The decelerated bubble acts as an obstruction in the flow path of the continuous flow and as a result, imposes a negative velocity gradient to the liquid and reduces its speed as is shown in Figure 5(b). After the breakup, mother bubble accelerates in the channel throat and finally attaches to daughter bubble that has a proportionally smaller volume of gas. At this instance, the front of the mother bubble, which is already attached to the rear of daughter bubble, pushes it upward. This enforces a sufficient momentum to the continuous phase to recover its velocity in the downstream of channel and flow with an almost similar velocity as before the onset of necking.

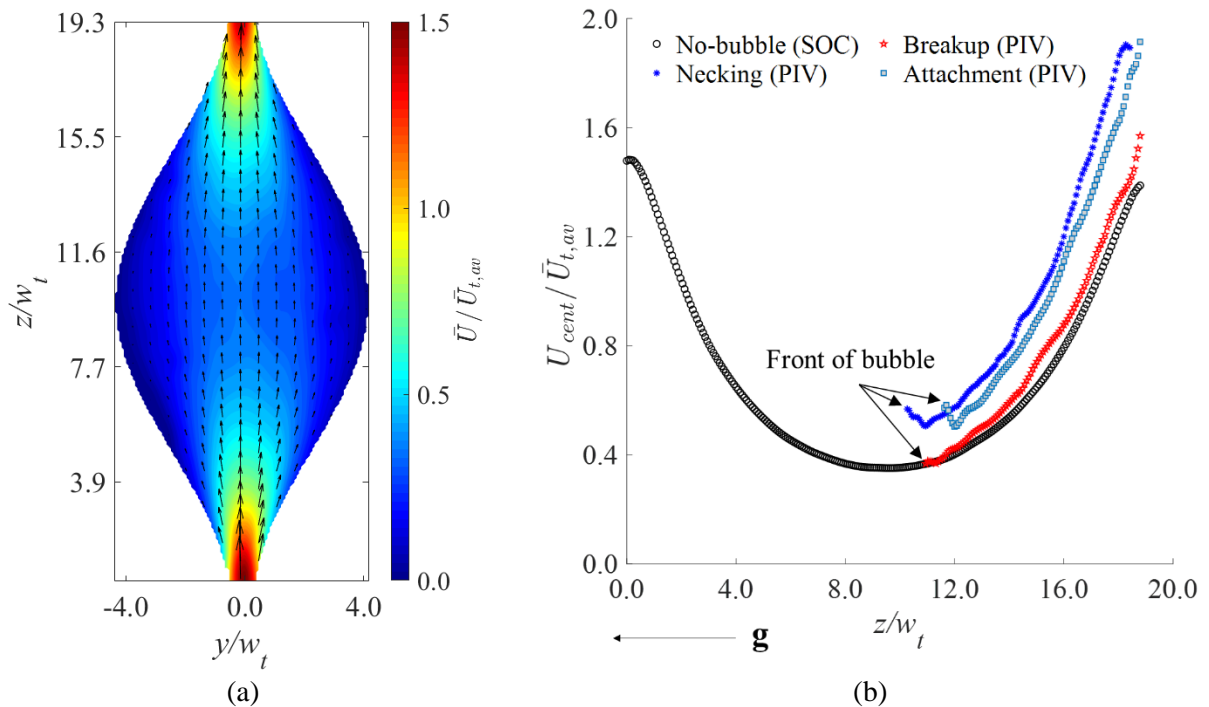


Figure 5: Calculated velocity field of (a) the single phase using the SOC algorithm and (b) the normalized velocity magnitude on the centerline of one full, wavy channel cycle for  $Q_1 = 342$  ml/h.

The viscous drag, surface tension, inertial, buoyancy and gravitational forces are the main forces which contribute to the dynamic behavior of the bubble as it passes constrictions (Lin et al., 2019). The order of dominance of these forces can be understood by calculating corresponding non-dimensional numbers. Table 1 lists the values of the main non-dimensional parameters that affect the topology and dynamic of the flow field. The values of Bond and Eotvos numbers are much smaller than unity meaning that the order of magnitude of buoyancy and gravitational forces are small in comparison to the surface tension force and can be neglected. Reynolds number and Weber number are calculated to be 0.389 and 0.334, respectively and shows the dominance of viscous and surface tension forces over the inertial forces. However, based on these values the inertia is still effective. The ratio of viscous to surface tension forces is defined based on the Capillary number with a value of 0.857

for the characteristic velocity of  $\bar{U}_{t,av}$ . This value shows that the viscous and capillary forces are in a close competition to overcome the other one. As a result of this analysis, the Capillary number is the most significant non-dimensional parameter for the current experiment with Reynolds and Weber numbers as effective, but less significant parameters.

Table 1 Definition of contributing non-dimensional numbers in the flow behavior

Ca	Re	Bo	Eo	We
$\frac{\mu_c \bar{U}_{t,av}}{\sigma}$	$\frac{\rho_c \bar{U}_{t,av} w_t}{\mu_c}$	$\frac{\rho_c g w_t^2}{\sigma}$	$\frac{\Delta \rho g w_t^2}{\sigma}$	$\frac{\rho_c \bar{U}_{t,av}^2 w_t}{\sigma}$
viscous/surface tension	inertia/viscous	buoyancy/surface tension	gravity/surface tension	inertia/surface tension
0.857	0.389	0.045	0.045	0.334

Figure 6 plots the temporal variation of velocity at the bubble front, at outlet throat and three streamwise positions at the channel centerline. The shown velocity magnitudes are averaged in a 3×3 stencil at each probing point. For all probe points, velocity magnitudes are almost constant before the bubble starts to neck down. Velocity profiles of throat and bubble front show noticeable fluctuations in contrast to the other probe points. These regions have the maximum uncertainty values of 15.17  $\mu\text{m}$  and 4.32  $\mu\text{m}$ , respectively which could be the main reason of these fluctuations. As the width of the bubble starts to shrink at the minimum cross-sectional area of the channel, the velocity of both bubble and continuous phase reduce significantly until the bubble collapses and a new daughter bubble is born.

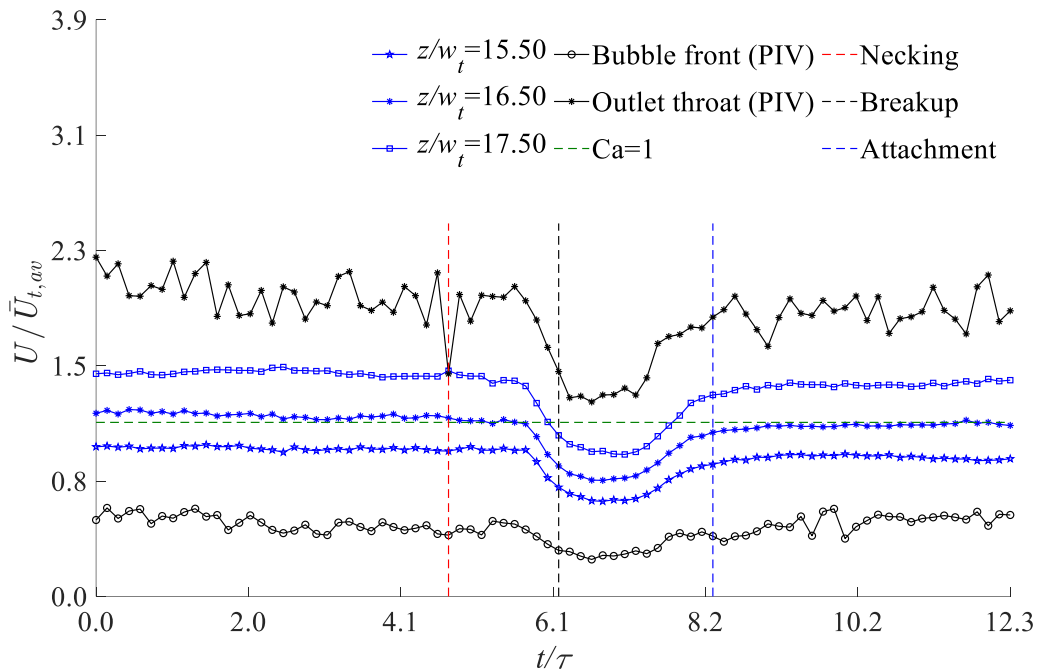


Figure 6: Temporal variation of normalized velocity of channel centerline.  $Q_1 = 342 \text{ ml/h}$ .

Tracking the behavior of the daughter bubble and bulk liquid, the velocities reduce to a minimum value before the mother bubble attaches to the daughter bubble and enforce a momentum to the flow field to recover the velocity. As shown in Figure 6, at the attachment inception bubble moves with a velocity lower than the flow field meaning that viscous drag forces are dominating the surface tension forces, which results in Capillary numbers less than unity. The Capillary number can be used to calculate the critical value of the characteristic velocity for which the viscous and surface tension

forces are equal. This normalized critical value equals  $U_{cr} = \sigma/\mu c \bar{U}_{t,av} = 1.166$  which is normalized with the characteristic velocity,  $\bar{U}_{t,av}$ . For velocity values more than  $U_{cr}$ , the viscous force is more dominant and the surface of the bubble tends to deform due to viscous drags.

## Conclusion

The experimental results show that monodisperse bubbles with sizes larger than the throat size experience three levels of dynamic transports while passing the minimum width of wavy channels: Necking, breakup and attachment. Necking starts while the viscous drag force hinders the rear of bubble to accelerate, while the front of bubble has already accelerated in the channel throat. The direct impact of necking is a significant reduction in the velocity of the surrounding liquid. During the breakup process, the flow field slows down to a critical value after which the attachment of mother to daughter bubble imposes a sufficient momentum to the flow field to recover its velocity back to values of the same order of velocity field before the necking inception. Calculation of the most relevant non-dimensional numbers show that Capillary, Reynolds and Weber numbers are the three significant parameters that control the behavior of the flow field.

## Acknowledgements

The authors gratefully acknowledge financial support from Natural Sciences and Engineering Research Council (NSERC) of Canada and RGL Reservoir Management Inc.

## References

- Cheng NS (2008) Formula for the viscosity of a glycerol-water mixture. *Industrial and Engineering Chemistry Research* 47:3285–3288.
- Cubaud T, and Ho C-M (2004) Transport of bubbles in square microchannels. *Physics of Fluids* 16:4575–4585.
- Krishna R, Urseanu MI, van Baten JM, and Ellenberger J (1999) Wall effects on the rise of single gas bubbles in liquids. *International Communications in Heat and Mass Transfer* 26:781–790.
- Lauga E, Stroock AD, and Stone HA (2004) Three-dimensional flows in slowly varying planar geometries. *Physics of Fluids* 16:3051–3062.
- Lin X, Bao F, Tu C, Yin Z, Gao X, and Lin J (2019) Dynamics of bubble formation in highly viscous liquid in co-flowing microfluidic device. *Microfluidics and Nanofluidics* 23:74.
- Liu X, Zhang C, Yu W, Deng Z, and Chen Y (2016) Bubble breakup in a microfluidic T-junction. *Science Bulletin* 61:811–824.
- Patel T, Patel D, Thakkar N, and Lakdawala A (2019) A numerical study on bubble dynamics in sinusoidal channels. *Physics of Fluids* 31:052103.
- Sauzade M, and Cubaud T (2013) Initial microfluidic dissolution regime of CO<sub>2</sub> bubbles in viscous oils. *Physical Review E - Statistical, Nonlinear, and Soft Matter Physics* 88:051001.
- Sauzade M, and Cubaud T (2018) Bubble deformations and segmented flows in corrugated microchannels at large capillary numbers. *Physical Review Fluids* 3:034202.
- Zhang C, Fu T, Zhu C, Jiang S, Ma Y, and Li HZ (2017) Dynamics of bubble formation in highly viscous liquids in a flow-focusing device. *Chemical Engineering Science* 172:278–285.
- Zhang Z, Drapaca C, Chen X, and Xu J (2017) Droplet squeezing through a narrow constriction: Minimum impulse and critical velocity. *Physics of Fluids* 29:072102.